Electronic Supplementary Material (ESI) for Energy & Environmental Science.

Supplementary Information for

Spatially isolating salt crystallisation from water evaporation for continuous solar-driven steam generation and salt harvesting

Yun Xia,[a] Qinfu Hou,[a] Hasan Jubaer,[a] Yang Li,[a] Yuan Kang,[a] Shi Yuan,[a] Huiyuan Liu,[a] Meng Wai Woo,[a] Lian Zhang,[a] Li Gao,[b] Huanting Wang,[a] Xiwang Zhang*[a]

[a] Department of Chemical Engineering, Monash University, Clayton, VIC, Australia. Email: xiwang.zhang@monash.edu

[b] *South East Water Corporation, PO Box 2268, Seaford Victoria 3198, Australia*

This PDF file includes:

1. Materials and Methods
2. Computational fluid dynamics modelling
3. Numerical simulation
4. Supplementary Notes 1 (Relationship between water transport and steam generation)
5. Supplementary Notes 2 (Demonstration with mixed salt solution and real seawater)
6. Supplementary Figures (Fig. S1-S26)
7. Reference

1. Materials and Methods

1.1 Materials

Carbon nanotubes (CNTs) powder, produced by chemical vapour deposition method, was supplied by Chengdu Organic Chemicals Co. Ltd. and used without further treatment. The outside diameter of the CNTs is smaller than 8 nm, and the length ranges between 10 and 30 µm. Filter papers with medium filter speed, supplied by Hangzhou Xinhua Paper Industry CO., Ltd., was employed as the substrate. The SEM images of the filter papers suggested that the diameter of cellulosic fibres is about 17 µm and the width of pores is in the range of 10 µm ~ 80 µm (Fig. S1a). A coil of black cotton thread with the diameter of ~1 mm (310 Nº 5) was supplied by the DMC Corporation. A piece of polystyrene foam bought from a local grocery shop was employed for thermal insulation. Its SEM image suggests that this foam is highly porous and the average pore size is about 130 µm. A piece of steel needle with a diameter of around 1 mm was employed to lead the cotton thread.

The chemicals sodium dodecylbenzene sulfonate (SDBS, flakes), Sodium Chloride (>99.5%), Magnesium chloride (≥98%), Calcium chloride (≥98%), Lithium chloride (≥99%), copper(II) sulphate pentahydrate (≥98%), Potassium Chloride (≥99%), Cobalt Chloride hexahydrate (≥98%) and Sodium Sulphate (≥99%) were supplied by the Sigma-Aldrich Pty Ltd and used as received without further treatment.

1.2 Preparation of CNTs suspension

To help the CNTs well dispersed in water, sodium dodecylbenzene sulfonate (SDBS) was chosen as the surfactant in preparing CNTs suspension[1, 2]. In typical, the CNTs/SDBS ration was 1:10 and the concentration of CNTs was 1 mg/mL. The SDBS and CNTs were added in DI water (resistivity 18 MΩ·cm) in sequence and followed with ultrasonication (Q500, QSonica Limited Liability Company) over 30 min to form a stable suspension (see Fig. S14a). This suspension was then sealed in a glass bottle for future use.

1.3 Preparation of evaporation disc

The evaporation disc was prepared by filtration of diluted CNTs suspension using filter paper. Unless otherwise specified, the vacuum filtration equipment was employed in the preparation and the suction area was a circle with a diameter of 4 cm. The loading amount of CNTs on filter paper was kept at 0.25 mg/cm^2 in this work. Thus, the required amount of the initial CNTs suspension (V, mL) was calculated based on the diameter of the suction area (D, cm) according to Equation S-1:

$$V = \frac{\pi \times (\frac{D}{2})^2 \times C_1}{C_0} \tag{S- 1}$$

Where C_0 is the initial concentration of CNTs in dispersion (mg/mL), C_1 is the loading of CNTs on filter paper (mg/cm^2).

The calculated amount of 1 mg/mL CNTs suspension was then diluted with DI water to 300 ml and followed with ultrasonication (ultrasonic bath cleaner, DOVES) for 10 min before use (Fig. S14b). A filter paper which can entirely cover the filtering area was used to retain and support CNTs from the suspension. After filtration, the uncovered part of filter paper was cut off. The self-assembled CNTs under vacuum constituted the light-absorbing layer while the underlying filter paper was used to absorb and transport water. These two layers constitute the evaporation disc.

1.4 Assembly of the solar steam generator

The assembly procedure is shown in Fig. S2. Briefly, the steel needle was employed to lead the cotton thread through the polystyrene foam and the as-prepared evaporation disc in sequence. Afterwards, a knot was tied at the top of the thread to immobilise the cotton thread on the surface of the evaporation disc. The total length of the cotton thread was about 10 cm to allow for solution transport to the evaporation disc from the bulk water. To minimise the effect of evaporation from the water surface, the polystyrene foam was cut to fully cover the container.

1.5 Solar evaporation test

The experimental setup can be found in Fig. S15**a**. To initiate the testing system, the solar steam generator was placed on the container with the cotton thread soaking in water. The solar light simulator was then turned on when the wetting mark reached the edge. The solar desalination system was placed under a Xenon light source (66912, Newport Corporation) and the mass profile with time was recorded every 10 seconds with an electronic balance (FZ-300i, A&D Weighing). Before every run, the light intensity of solar simulator was adjusted to 1000 w/m^2 (one sun) via calibrating with a thermopile sensor (919P-010-16, Newport Corporation) connected to a light metre (843-R-USB, Newport Corporation). To minimise the error from the uneven distribution, the solar flux at over five separated locations was measured and then averaged. An infrared camera (TI100, Fluke Pty Ltd) was employed for recording the temperature of the system. The temperature data were obtained by averaging the temperature of whole area evaporation disc via SmartView® Infrared Imaging Analysis and Reporting Software. The solar evaporation experiments were conducted in an environment with an ambient temperature around 22°C and relative humidity of approximately 50%. The same procedure was followed to conduct the control experiments without the solar steam generator. To investigate the effect of disc area on evaporation performance, the evaporation disc was firstly cut according to the required diameter and its accurate area was then measured with ImageJ software. The evaporation rate in the dark was measured under a cardboard box (24 cm × 24 cm × 24 cm), and the mass profile was measured every 10 seconds with the electronic balance.

1.6 Calculation of solar to vapour & salt conversion efficiency

The solar to vapour and salt efficiency (η_{VS}) was calculated as follows:

$$\eta_{VS} = \frac{\dot{m} \times (H_{LV} + W_{least})}{Q_i}$$

where $\dot{m}$ is the as-measured water evaporation rate generated by the solar steam generator (kg/m^{2}h, total water evaporation subtracts the natural evaporation without solar light irradiation); Q_i donates the solar light intensity reaching on the device every hour(1 kW/m^{2}h) and the H_{LV} is the overall enthalpy change of the liquid-vapour phase transition (2,257 kJ/kg). W_{least} represents for the theoretical least work to separate the salt solution into solid salts and pure water according to the literature[3], it is reported that the energy consumption for separating 35 g/kg NaCl solution into pure water and solid salt is 10.75 kJ/kg feed, equal to 10.39 kJ/kg water (we took it as an approximate value for 35 g/L NaCl solution).

As shown in Fig. 2d, the water evaporation rate from 35 g/L NaCl solution for 4 cm and 1.5 cm disc was measured to be 1.05 kg/m^{2}h and 1.42 kg/m^{2}h, respectively. Subtracting the dark evaporation (0.13 kg/m^{2}h, Fig. S13b), the solar light-induced evaporation rate for the 4 cm disc and 1.5 cm disc are 0.92 kg/m^{2}h and 1.29 kg/m^{2}h, separately. According to the above equation, the solar to vapour and salt conversion efficiency was calculated to be 57.9% for the 4 cm disc and 81.2% for the 1.5 cm disc.

1.7 Measuring the effective porosity of the evaporation disc

Before assembling the solar steam generator, the evaporation disc with a diameter of 4 cm was firstly weighted by an analytical balance (HR-250AZ, A&D Company). After wetting in water for 2 hours, the evaporation disc was carefully detached and weight again. The effective porosity of the evaporation disc (Φ) can be calculated as below:

$$\Phi = \frac{(m_2 - m_1)/\rho_2}{m_1/\rho_1 + (m_2 - m_1)/\rho_2} \qquad (S\text{-}2)$$

Where m_1 and m_2 are the weight of evaporation disc before and after wetting (mg), respectively; ρ_1 and ρ_2 are the density of cellulose (1.5 g/cm^2) and water (1 g/cm^2), respectively.

1.8 Salt distribution measurement

Salt concentration data was obtained by cutting a small area from the evaporation disc and followed with measuring the total amount of salt. Before assembling the solar steam generator, a grid was drawn on the back of the evaporation disc (Fig. S16). The rest of the preparation method, as well as the assembly process, is the same as above. After running the experiment for ten minutes, the evaporation layer was immediately detached from the system, and five samples on each side were cut from the layer along the predesigned grid. Afterwards, all the flakes were recorded by the digital picture for area calculation using ImageJ software. These samples were then immersed in 5 ml DI water for over 12 hours with constant shaking. The concentration of the leaching solution was then determined by a conductivity meter (labCHEM). The mass fraction of salt (ω) can be calculated as below:

$$\omega = \frac{C \times V}{A \times (\frac{m_2 - m_1}{A_0})} \qquad (S\text{-}3)$$

Where C is the NaCl concentration of the leaching solution (mg/mL), V is the volume of the leaching solution (mL), A is the area of the sample (cm^2), A_0 is the area of evaporation disc (cm^2), m_1 and m_2 are the weight of evaporation disc before and after wetting (mg), respectively.

1.9 Controllable crystallisation

Two more configurations of solar desalination were tested in this paper. The first configuration was with two cotton threads at the opposite sides of the edge, as shown in Fig. S5**b**. The second configuration was with four cotton threads dividing the edge into for even parts (Fig. S5c). The assembling process and experimental details were the same as the configuration with one thread in the centre. 35 g/L NaCl solution was used for crystallisation in this part. Time-lapse photography was employed during the experiments at one frame per minute.

1.10 Weight change profile in the wetting process

Before the experiment, the evaporation disc in the dry state was weighed and then connected with a cotton thread. Another side of the cotton thread was then put in DI water, and we started a stopwatch. The evaporation disc was taken out and weighed every 5 min during the first hour and then measured again after 15 hours. The relative weight (φ) was calculated as below:

$$\varphi = \frac{m}{m_0} \times 100\% \qquad (S\text{-}4)$$

Where m_0 is the weight of evaporation disc in dry state and m is the weight at the different time.

1.11 Long-time evaporation and salt harvesting experiment

Before starting the experiment, i.e. placing the device under solar light, the desalination system was left for over 6 hours to allow for thoroughly wetting the disc. In order to reduce the refilling operation during crystallisation experiment, a larger beaker with a volume capacity of 300 ml (Fig. S15**b**) was employed to hold saline water, and the diameter of evaporation disc was reduced to 2 cm. Note that the larger beaker was firstly sealed with a piece of polystyrene foam to minimize the influence of the natural evaporation by the water surface. Therefore, the smaller disc area can be used to calculate the weight loss rate. Time-lapse photography was employed during each run at one frame per minute and videos were created from the recording at 30 frames per second. In this part, the mass profile of the system was recorded every minute. The crystallised NaCl was collected directly from the collecting platform around every 100 hours. The collected salt was then dried in an oven at 60°C for over 24 hours. The weight was measured after drying, in order to eliminate the moisture content.

The control experiment employed air-laid papers wrapping the PS foam for water transportation. As demonstrated in Fig. S17**a**, the water was firstly transported upwards through the paper and then spread from the edge to the inner part. Fig. S17**b** shows the experiment set-up at the initial stage.

1.12 Water collection experiment

A home-made solar still was employed for water collection. The experimental setup is shown in Fig. S18. The dimension of the glass dome is 15 cm in diameter and 27 cm in height. The device array composed of thirteen 1.8 cm evaporation discs was employed for this demonstration. The whole system was put under placed under a larger Xenon light source (CHF-XM500, Perfect Light). The light intensity was adjusted to 1000 w/m^2 (one sun) before the experiment. To minimise the error from the uneven distribution, the solar flux at over five separated locations was measured and then averaged. The water samples were collected with Pasteur pipette every two hours. The ion concentrations of all the samples were tested by inductively coupled plasma mass spectrometry (ICP-MS, Perkin Elmer Optima 7000 DV).

1.13 Characterization

The morphology and thickness of the materials were recorded using an FEI Nova Nano450 SEM at 5 kV accelerating voltage, where all the samples were attached to carbon tapes and coated with Iridium. The contact angles of filter paper and polystyrene foam were measured by a contact angle measuring device (OCAH-230, Dataphysics Company) with three µL dosing amount. The Light absorption of the top of evaporation disc (in the range of 250~2500 nm) was measured with a UV/VIS/NIR spectrometer (950 PerkinElmer Lambda) attached to an integrating sphere, in which the sample had been placed. The concentration of ions in solution was analysed by inductively coupled plasma atomic emission spectroscopy (ICP-AES, Perkin Elmer Optima 7000).

2. Computational fluid dynamics modelling

2.1 Geometry and mesh generation

The model geometries are created in the software Gambit 2.4.6 according to the experiments (Fig. S19a) where the disc thickness is 0.107 mm for the water-spreading layer, and its diameter is 40 mm. To save computational cost, the calculation domains are chosen for the discs with one, two and four threads (see, Fig. S19b-d), considering the symmetry for two and four threads cases. Thus, for the cylindrical geometry, there are top, bottom, side (for one thread case), and symmetrical (for the two and four threads cases) surfaces.

The dependence of mesh size is examined with 4, 6, 8, and 10 intervals in the thickness direction and the other parts were meshed with a similar mesh size as did in the thickness direction correspondingly. For 6, 8 and 10 intervals, the variation of the result is negligible. Specifically, for the one thread case, the inside circle is divided into 200 intervals, and there are ten intervals in the thickness direction. The outside circle is also divided into 200 intervals so that a regular map-type mesh can be generated for the geometry which benefits the accuracy and convergence of the simulations. The interval size in the radial direction is 0.025 mm. There are 24,800 elements in total. For two and four threads cases the mesh sizes are general of the same size and special attention is made to divide the arc around the inlet. There are 25,110 elements for the two-thread case and 11,667 elements for the four-thread case (because only a quarter of the domain is considered for the symmetrical geometry).

2.2 Multiphase mixture model and boundary conditions

A CFD model is formulated by using the commercial software CFX 17.1 to understand the saline water evaporation process. The mesh generated is first loaded into CFX-Pre 17.1 where various multiphase models can be selected and boundary conditions are set. The mixture model with two species: water and salt are chosen because both of them are in the liquid state (before reaching the saturation of the salt). According to the experiments the temperature variation is insignificant, and therefore no energy conservation equation is solved for simplification. The small Reynolds number ($Re = \rho uL/\mu$ = 131.46, calculated with water density ρ = 997 kg/m^3, water dynamic viscosity μ = 0.00089 Pa, the calculated inlet water velocity u = 0.00117 m/s (according to the measured evaporation rate 1.05 kg/m^{2}h) and the water-spreading layer thickness *L* = 0.107 mm) allows us to use the laminar flow model. Hence, the conservations of mass and momentum over a computational cell are given by:

$$\partial(\rho_a \varepsilon_a)/\partial t + \nabla \cdot (\rho_a \varepsilon_a \mathbf{u}) = S_a \qquad \textit{(S- 5)}$$

$$\sum_1^2 \varepsilon_a = 1 \qquad \text{(S- 6)}$$

and

$$\partial(\rho_a \varepsilon_a \mathbf{u})/\partial t + \nabla \cdot (\rho_a \varepsilon_a \mathbf{u}\mathbf{u}) = -\varepsilon_a \nabla p + \nabla \cdot \tau + M_a \qquad \textit{(S- 7)}$$

where S_a represents the mass source due to water evaporation and M_a for momentum sources due to body forces and τ for stress tensor.

Then, the boundary conditions are set in CFX-Pre 17.1. The inlet is set as a pressure inlet with zero static pressure and the mass fraction of the salt at the inlet is 96.62% (mass concentration of salt is 3.38%, corresponding to the 35 g/L NaCl solution). Note that the velocity inlet condition was tested and it was difficult to reach the balance between the evaporation and inlet water mass fluxes. The outlet (side wall) boundary is set without flow according to the experiments. Hence, the water loss is only through the evaporation at the top surface, where a surface source term is included to represent water evaporation and the water mass flux is set according to the experimental measurement and the local water mass fraction (the evaporation rate from the experimental measurement is 1.05 kg/m^{2}h, and thus, the expression of the surface evaporation flux for the 40 mm disc is -0.000292 × WaterMassFraction, and the unit is kg/m^{2}s). The initial mass fraction of water (96.62%) in the whole domain is set according to the pre-wetted condition by saline water.

For the experiments, the water-spreading layer plays an important role in the transport of the liquid mixture, and the capillary force in a porous medium is involved. It is a challenge for the CFD to model such a mechanism and that is one reason why a pressure inlet boundary condition is adopted. It should be noted that the evaporation rate and the water flow rate at the pressure inlet are equal because the outlet velocity is set as zero according to the experiments. For the two and four threads cases symmetrical boundaries are set.

Based on the mixture model and boundary conditions, the multiphase flow field can be solved by CFX-Solver 17.1 with a transient calculation model with a time step of 1 s (a case with a smaller time step 0.1 second was run and no significant difference was observed). Because of the small scale of the geometry/mesh size and the operational parameters including the evaporation rate and the inlet water velocity double precision calculation is adopted. The salt mass concentration and the flow streamline are demonstrated in the main Fig. 3. Because the current model does not consider the crystallization of salt the model will run until the highest salt mass fraction reaches the crystallization concentration (26.52%) at around 1,000 s for the given conditions. For convenience, Table S1 lists the key settings used in the simulation.

Table S1 Key settings for the CFD model

Boundary conditions	
Initial water (salt) mass fraction	96.62% (3.38%)
Pressure at the inlet	0
Material properties	
Salt diffusion coefficient	1.5e-9 m^2/s
Salt density	2,000 kg/m^3
Salt dynamic viscosity	1 Pa˙s
Water density	997 kg/m^3
Water dynamic viscosity	8.9e-4 Pa˙s
Solver parameters	
Analysis type	Transient, double precision
Time step	1 s
Residual target	1e-8
Max iterations per loop	10
Total time	1,000 s

3. Numerical simulation

3.1 Model details

The process of water transport and salt accumulation can be demonstrated as shown in Fig. S20. The evaporation disk was divided into an unlimited number of cells. The mass transfer of cell N includes three parts: advection, diffusion and evaporation. The following form of the general transport equation for solute transport through a system subjected to advection-diffusion is well known:

$$\frac{\partial c}{\partial t} = \nabla.(D\,\nabla c) - \nabla(\vec{v}c) + S \qquad (S\text{- }8)$$

Where,

c=concentration of solute;

D=Diffusion coefficient=1.5×10^{-9} m^2/s [4]

$\vec{v}$=velocity of the fluid;

S=Source term due to generation or dissipation

For only a radial transport on a cylindrical coordinate system, the transport equation can then be expressed as:

$$\frac{\partial c}{\partial t} = \frac{1}{\mathrm{r}}\, D\,\frac{\partial}{\partial r}\left(r\frac{\partial c}{\partial r}\right) - \vec{v}\frac{\partial c}{\partial r} + S \qquad (S\text{- }9)$$

The source term in this equation can be utilised to account for the change in concentration due to evaporation. While the change in mass of water due to evaporation can be determined by employing the following equation, we take the evaporation flux value that was experimentally determined:

$$\frac{dm_w}{dt} = h_m A_{surf}\left(\rho_{i,surf} - \rho_{i,\infty}\right) \leftarrow experimentally\ determined \qquad (S\text{- }10)$$

$$\frac{dm_w}{dt} = A_{surf}\dot{F}_{exp} \qquad (S\text{- }11)$$

Where,

$\dot{F}_{exp}$=Area specific evaporation rate (experimentally determined)

A_{surf}=Surface area participating in evaporation

The difficulty lies in transferring information obtained from the water evaporation into the change in concentration of the solute.

Therefore, at any particular instance, for which the solute mass is constant, inside of a control volume the following relationship can be derived, while due to evaporation the solute concentration changes:

$$c = \frac{M_s}{M_w + M_s} \tag{S- 12}$$

$$\frac{\partial M_w}{\partial c} + 0 = -\frac{M_s}{c^2} \tag{S- 13}$$

Therefore, with the extension of the temporal derivative of concentration by means of the chain rule, we get:

$$\frac{\partial c}{\partial t} = \frac{\partial c}{\partial M_w}\frac{\partial M_w}{\partial t} = -\frac{c^2}{M_s}\frac{\partial M_w}{\partial t} = -\frac{c^2}{M_s}A_{surf}\dot{F}_{exp} \tag{S- 14}$$

By replacing the source term in the transport equation with this temporal change in concentration we finally get:

$$\frac{\partial c}{\partial t} = \frac{1}{\mathrm{r}}\, D\frac{\partial}{\partial r}\left(r\frac{\partial c}{\partial r}\right) - \vec{v}\frac{\partial c}{\partial r} - \frac{c^2}{M_s}A_{surf}\dot{F}_{exp} \tag{S- 15}$$

The mass of salt M_s in the control volume can be replaced as follows:

$$M_s = M_{total} \times c = V \times \rho \times \varepsilon \times c \tag{S- 16}$$

Where,

V=Volume of the control volume

ρ =Density of the solution / fluid mixture

ε=Porosity of the control volume

With this substitution the transport equation finally takes the following form:

$$\frac{\partial c}{\partial t} = \frac{1}{\mathrm{r}} D \frac{\partial}{\partial r}\left(r \frac{\partial c}{\partial r}\right) + \vec{v} \frac{\partial c}{\partial r} + \frac{c}{V \times \rho \times \varepsilon} A_{surf} \dot{F}_{exp} \qquad \textit{(S- 17)}$$

The velocity vector can be calculated based on the steady state mass balance for a control volume, which then can be solved in the discretised domain for each element to find the volume flow rate and hence the velocity:

$$\dot{M}_{in} = \dot{M}_v + \dot{M}_{out} \qquad \textit{(S- 18)}$$

Where $\dot{M}_v$ is the mass loss due to evaporation, i.e. $A_{surf} \dot{F}_{exp}$. The mass balance of each element can be expressed as:

$$A_{flux_{in}} v_{in} \varepsilon \, \rho_{in} = A_{surf} \dot{F}_{exp} + v_{out} \, A_{flux_{out}} \, \rho_{out}$$

$$=> v_{out} = \frac{A_{flux_{in}} v_{in} \varepsilon \, \rho_{in} - A_{surf} \dot{F}_{exp}}{A_{flux_{out}} \, \rho_{out}} \qquad \textit{(S- 19)}$$

In equation (S-16), both densities, i.e. ρ_{in} and ρ_{out} refer to those of the fluid mixture. Moreover, it is implied that the areal porosity porosity (2D) is the same as the volume based (3D) porosity used in equation (S-16). This is already proved to be true in literature[5].

As can be seen, the velocity is a function of density, which on the other hand is dependent on the actual salt concentration. Therefore, even though the mass balance of water originates from a steady state balance and hence is not time-dependent, the velocity will be varying with time as the concentration changes. As a result, velocity is required in order to solve the PDE to obtain the concentration profile and vice versa. Thus, these two equations - (S-14) and (S-16) - need to be coupled during the solution. However, the coupling can be referred to as "one-way coupling", because the fluid is affecting the salt concentration within each time step and then progressing in a segregated manner. Since the inlet velocity of the control volume is used in (S-14) and this only depends on the concentrations and parameters of the previous control volume, in addition to the fact that the velocity calculation is one temporal step ahead of the concentration solution, no iteration is required.

In order to solve the PDE, the field can be initialised with the constant inlet concentration of the bulk saline water:

$$c|_{(t=0,\ r)} = 0.0338$$

The boundary conditions that could be used to solve the partial differential equation are:

$$c|_{(t,\ r=0)} = 0.0338$$

3.2 Discretisation

The continuous form of the equation (S-14) is as follows:

$$\frac{\partial c}{\partial t} = \frac{1}{\mathrm{r}}\, D \frac{\partial}{\partial r}\left(r\frac{\partial c}{\partial r}\right) - \vec{v}\frac{\partial c}{\partial r} + \frac{c}{V \times \rho \times \varepsilon} A_{surf}\dot{F}_{exp}$$

If we apply it to a system with spatial discretization, for any cell j in the interior of the simulation domain, we get:

$$\frac{\Delta c_j}{\Delta t} = \frac{1}{\mathrm{r}}\, D \frac{\Delta}{\Delta r}\left(r\frac{\Delta c_j}{\Delta r}\right) - v_{j,in}\frac{\Delta c_j}{\Delta r} + \frac{c_j^n}{V \times \rho(c_j^n) \times \varepsilon} A_{surf}\dot{F}_{exp}\,\Delta t \tag{S- 20}$$

$$=> \frac{\Delta c_j}{\Delta t} = \frac{D}{\Delta r}\left[\frac{(c_{j+1} - c_j)}{\Delta r} - \frac{(c_j - c_{j-1})}{\Delta r}\right] - v_{j,in}\frac{(c_{j+1} - c_j)}{\Delta r} + \frac{c_j^n}{V \times \rho(c_j^n) \times \varepsilon} A_{surf}\dot{F}_{exp}\,\Delta t \tag{S- 21}$$

The temporal discretization then leads to for any time step n and time step factor Δt:

$$\begin{aligned} c_j^{n+1} = c_j^n + \frac{D}{\Delta r}\left[\frac{(c_{j+1}^n - c_j^n)}{\Delta r} - \frac{(c_j^n - c_{j-1}^n)}{\Delta r}\right]\Delta t - \ v_{j,in}\frac{(c_{j+1}^n - c_j^n)}{\Delta r}\Delta t \\ + \frac{c_j^n}{V \times \rho(c_j^n) \times \varepsilon} A_{surf}\dot{F}_{exp}\,\Delta t \end{aligned} \tag{S- 22}$$

The convective term was discretised using an apparent upwind scheme as the velocity was calculated for the inlet into the discretised cell using the following scheme:

$$v_{j,in}^n = v_{j-1,out}^n = \frac{A_{flux,in_{j-1}} v_{j-1,in}\, \varepsilon\, \rho_{j-2}(c_{j-2}^n) - A_{surf,j-1}\dot{F}_{exp}}{A_{flux,out_{j-1}}\, \rho_{j-1}(c_{j-1}^n)} \tag{S- 23}$$

This scheme requires a disparate approach to calculate the velocity in the leftmost boundary cell. This was determined from the mass flow inlet through the thread and the cross-section area of the thread:

$$v_0 = \frac{\dot{M}_{mix,0}}{2\pi r_{thread} h} \tag{S- 24}$$

3.3 Initial and Boundary Conditions

All the cells in the simulations domain will be initialised with the concentration of the bulk brine solution as the initial concentration $c_0|_{r=0} = 0.0338$.

At the left boundary of the model corresponding to the source of the brine solution entering the paper layer, a constant salt concentration was assumed. In the discretised form and corresponding to the experimental values,

$$c^n_{r=0.005} = 0.0338 \qquad \text{(Left boundary)}$$

At the right boundary of the model corresponding to the edge of the model, the only salt fluxes across the discretised cell are: diffusion to (and fro) form the preceding cell, upstream convective flux into the boundary cell. As there are no downstream cell for forwarding diffusion,

$$c^n_{r=0.02} = c^n_{j(r=0.02)-1} \qquad \text{(Right boundary)}$$

It is noteworthy that this form of numerical treatment enforces no downstream diffusion.

3.4 Simulation Methodology

The simulation was performed by using the commercial spreadsheet software Microsoft Excel. The geometry was assumed to be a disc of 4 cm diameter and 0.1 mm thickness. The mesh of the calculation domain was discretised using a spatial length scale of $1 \times 10^{-4}\ m$ following an analysis on mesh independence. The temporal discretisation utilized a time step size of 0.1 s.

The model was limited to the maximum salt concentration at the saturation and hence crystallization was not included in the calculation for simplification. As a result, the simulation was terminated as soon as the salt concentration reached saturation.

3.5 Simulation Validation and Discussion

The simulated results are validated by the experimental measurement (Fig. S21). The salt concentration increases with time at a different rate and the outer part of the disc reaches higher concentration than the inner part because of the progression evaporation during water transport (Fig. S22). Additionally, the velocity of salt solution flow through the filter paper decreases exponentially with the radial distance (Fig. S23), which further intensifies the steep salt gradient inside the evaporation disc.

4. Supplementary Notes 1 (Relationship between water transport and steam generation)

The steam generation rate as a function of disc size has been shown in Fig. S3a. We did additional experiments to better understand the reason why the water evaporation rate slightly decreases with increasing the disc size. We found that the initial water evaporation rate of the large disc after the pre-wetting is almost the same as that of the small disc. However, the evaporation rate of the large disc decreased at first 2400 s and then levelled off (Fig. S3b). We then measured the water content profile of the evaporation disc after the evaporation rate was stabilized. As shown in Fig. S3c, highest water content was observed in the area near the centre. From the centre to the edge, the water content gradually decreases due to the water transport limitation. The low content at the area far away from the centre slows down the water evaporation. Nevertheless, by increasing water transport, the water evaporation of large disc can be enhanced. As shown in Fig. S3d, higher water evaporation rates, 1.01 kg/m^{2}h and 1.25 kg/m^{2}h, were achieved on the devices with 4 layers and 8 layers filter paper, respectively, compared with 1 layer filter paper device (0.57 kg/m^{2}h).

5. Supplementary Notes 2 (Demonstration with mixed salt solution and real seawater)

According to the literature[6], the normal seawater mainly comprises of NaCl (35 g/L), and other main ions (2,701 mg/L) SO_4^{2-}, (1,295 mg/L) Mg^{2+}, (416 mg/L) Ca^{2+}, (390 mg/L) K^+ and (0.170 mg/L) Li^+. Based on the contents of these salts, we prepared 5 mixed salt solutions containing 35 g/L NaCl with 3 g/L Na_2SO_4, 5 g/L $MgCl_2$, 1 g/L $CaCl_2$, 0.8 g/L KCl or 1 g/L LiCl, respectively. As shown in Fig. S24a, these 5 samples showed similar water evaporation rate at the beginning. But their water evaporation rates had different trends with the operation time. The water evaporation of NaCl solutions with Na_2SO_4, KCl and LiCl were relatively stable, while those of the solutions with $MgCl_2$ and $CaCl_2$ gradually decreased. These phenomena can be ascribed to the different crystallization behaviour of the mixed salt. As shown in Fig. S24c)-h), the first group of salts (the mixture of NaCl with Na_2SO_4, KCl and LiCl, respectively) crystallized at the edge only while the second group of salts (the mixture of NaCl with $MgCl_2$ and $CaCl_2$, separately) gradually crystalized at the inner part and the evaporation disc was partially covered. The reason behind these phenomena is the different properties of their solution. Under the testing condition, the vapour pressure of saturated NaCl solution is around 3.33 kPa (30°C) while that of ambient environment is around 1.70 kPa (30°C, 40% humidity)[7]. In this case, water molecules can further evaporate from the saturated solution to the environment due to the vapour pressure difference, leading to the following crystallisation. On the contrary, the vapour pressure of saturated $MgCl_2$/$CaCl_2$ solution (1.33 kPa and 0.93 kPa at 30°C, respectively)[7] is lower than that of the ambient environment. It stops the solutions from further losing moisture and thus leads to the failure in crystallization. It is further confirmed by the experiment with MgCl2 and CaCl2 solutions, in which only gel-like solution can be found on the evaporation disc, as shown in Fig. S25.

From the perspective of molecular level, the interaction between ions and water molecules is believed to cause the difference nature of crystallization. As water molecules have strong molecular polarity, the charged ions have a certain level of attraction with the opposite-charged side of water molecule. This attraction normally increases with the ratio of the charge number to the radius of ions[8]. After the free water molecules evaporate away, the behaviour of bound water molecules will be depend on the attraction between ions and water molecules.

Under the circumstance, Na^+ will lose the bond water molecules because of the weak attraction due to its small z/R_i ratio (8.62 e/nm, Table S2), while Mg^{2+} and Ca^{2+} can retain the bound water molecules because of their high z/R_i ratio (23.26 e/nm and 17.54 e/nm, Table S2). Therefore, NaCl solution can crystallize under the testing conditions while $MgCl_2$ and $CaCl_2$ solution fail.

We then collected seawater samples (from Lacepede Bay, Australia) to show the performance with real seawater. Before the experiment, the seawater was filtered by Mixed Cellulose Ester membrane (MCE membrane, pore diameter 0.22 μm) to remove the suspended solids. To avoid the interference of $MgCl_2$ and $CaCl_2$, we pre-treated the seawater using ion-exchange () to remove them, which is one of the common processes in reverse osmosis seawater desalination plant. The water quality data before and after the pre-treatment are listed in Fig. 5e. Afterwards, the treated seawater was used for steam generation and salt crystallization. As shown in Fig. S26, the solar steam generator worked well for the pre-treated seawater. Stable water production and salt harvesting at the edge are achieved.

Table S2 The ion charge number and radius of the main cations in seawater

	Na	*Mg*	*Ca*	*K*	*Li*
z, Charges in water (e)	*+1*	*+2*	*+2*	*+1*	*+1*
R_i, Ionic radii[9] (nm)	*0.116*	*0.086*	*0.114*	*0.152*	*0.090*
z/R_i (e/nm)	*8.62*	*23.26*	*17.54*	*6.58*	*11.11*

6. Supplementary Figures (Fig. S1-S26)

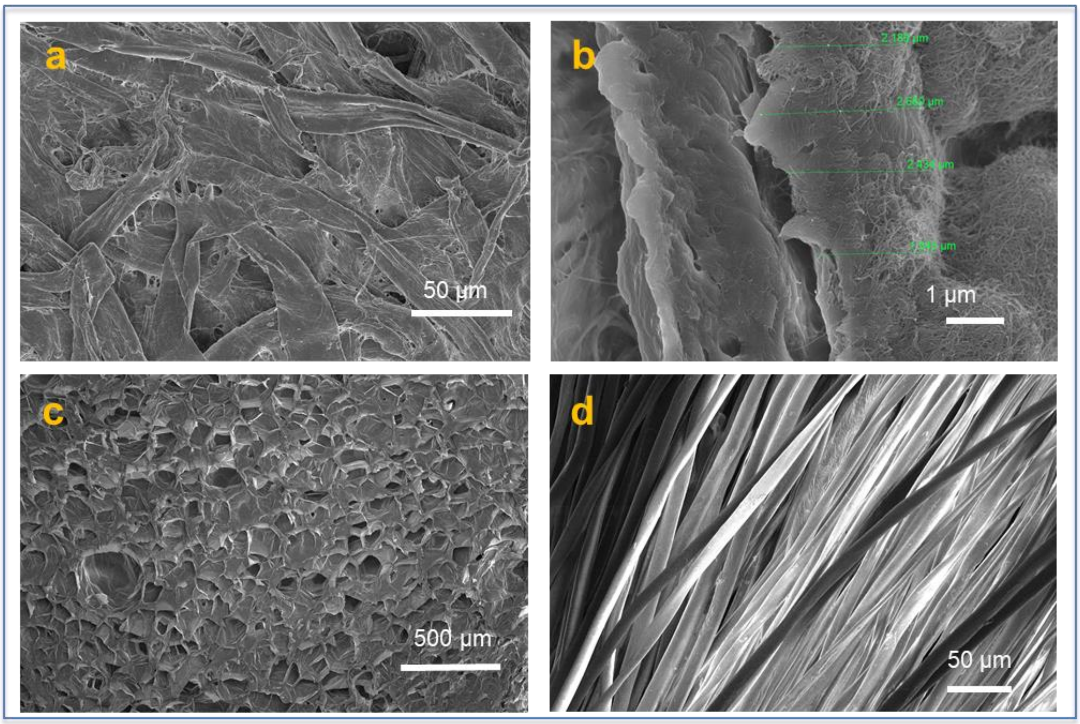

Fig. S1 SEM images of the components of solar steam generator. a) Top view of the filter paper (water-spreading layer). The average diameter of cellulose fibres is around 15 µm. b) Cross section of the CNTs layer (light-absorbing layer). The loading of CNTs is 0.25 mg/cm^{2,} *and the average thickness of the CNTs layer is about 2~3 µm. c) Cross section of polystyrene foam with very high porosity (insulating layer). The average pore size is approximately 130 µm. d) The side view of cotton thread (water-transport thread). The average diameter of cotton fibres is around 10 µm.*

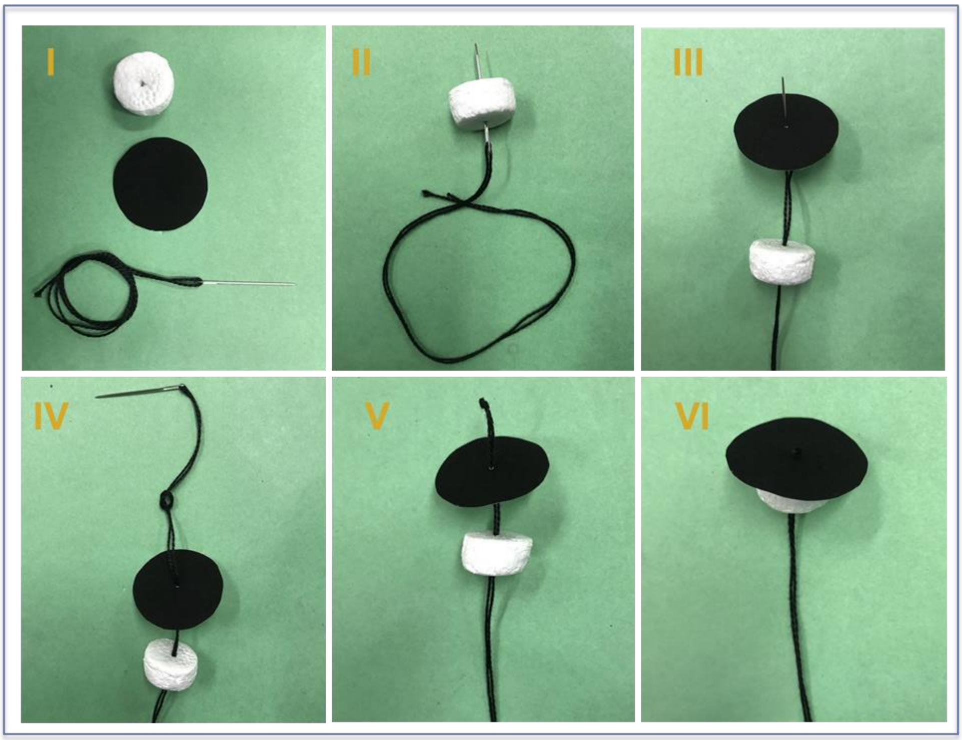

Fig. S2 Step-by-step fabrication of the solar desalination system. (I) Prepare the four components-polystyrene foam, evaporation disc, cotton thread and needle. (II) Use the needle to lead cotton thread through the polystyrene foam. (III) Use the needle to lead cotton thread slowly through the evaporation disc. (IV) Tie a knot on top of the evaporation disc and make sure there was enough thread under the foam (the length under the knot was about 10 cm). (V) Cut the thread over the knot. (VI) Slowly pull the cotton thread under the foam till the knot reach the evaporation disc.

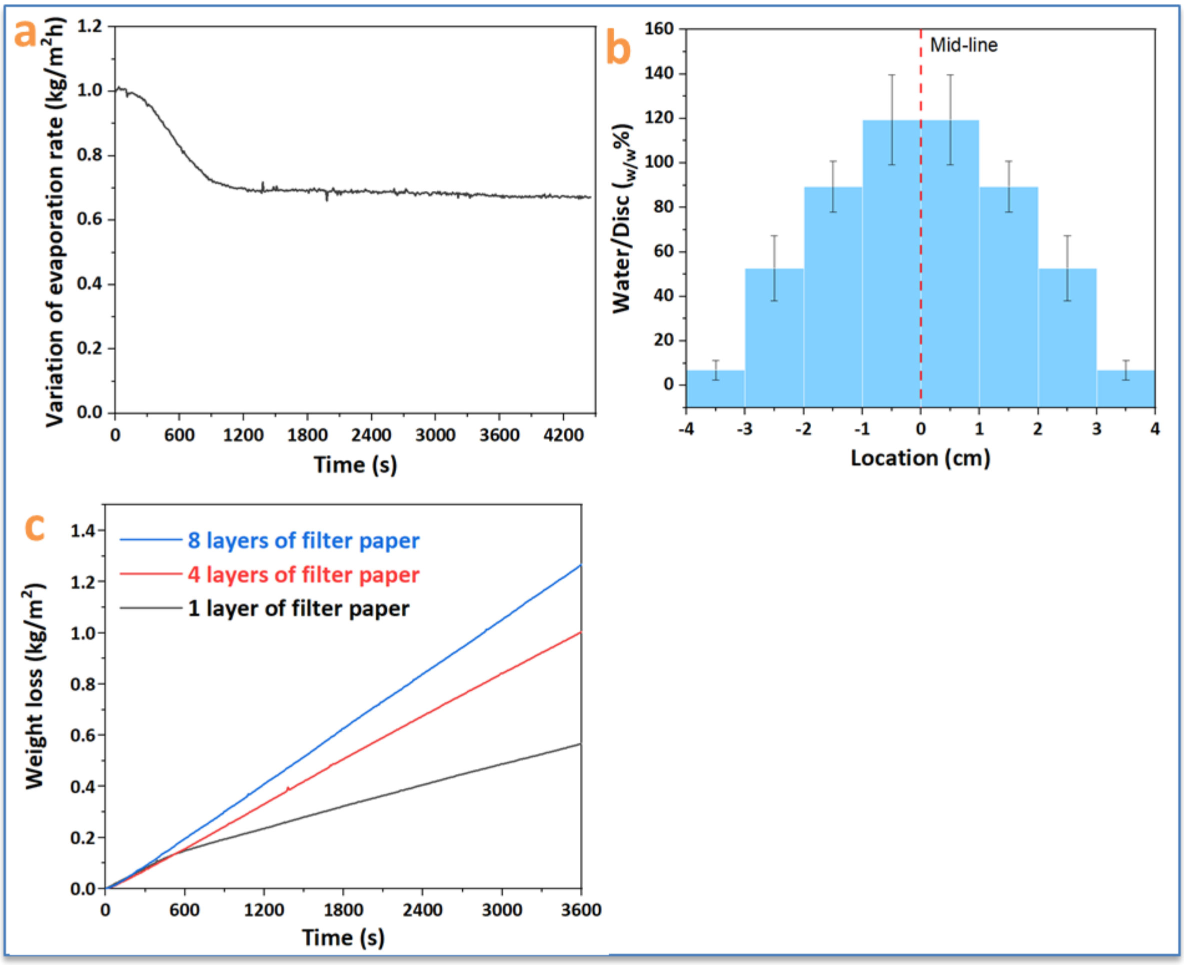

Fig. S3 The water evaporation on the 8cm evaporation disc. a) The variation of evaporation rate with the 8 cm evaporation disc under one sun. b) The as measured water content at different locations. c) Water evaporation performance of 8 cm evaporation disc with 1, 4 and 8 layers of filter paper..

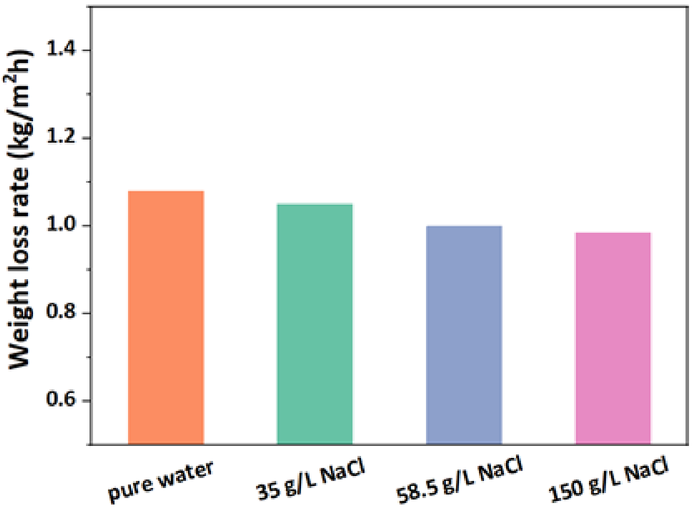

Fig. S4 Effect of salt concentration on the evaporation rate. This series of experiment was conducted with the D=4 cm evaporation disc under one sun. The water evaporation rate decreases with the salt concentration, which can be attributed to the drop in water vapour pressure at high salt concentration.

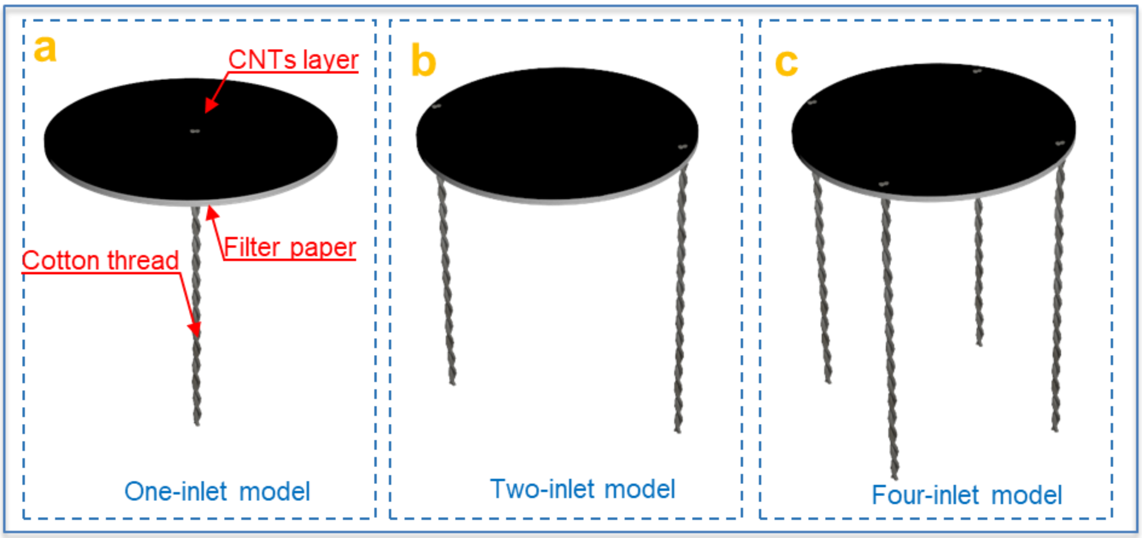

Fig. S5 Illustration of one-inlet (a), two-inlet (b), and four-inlet (c) configurations. Except for the number and location of cotton threads, other parameters, such as the evaporation disc and cotton thread, were the same as the "one-pump" system.

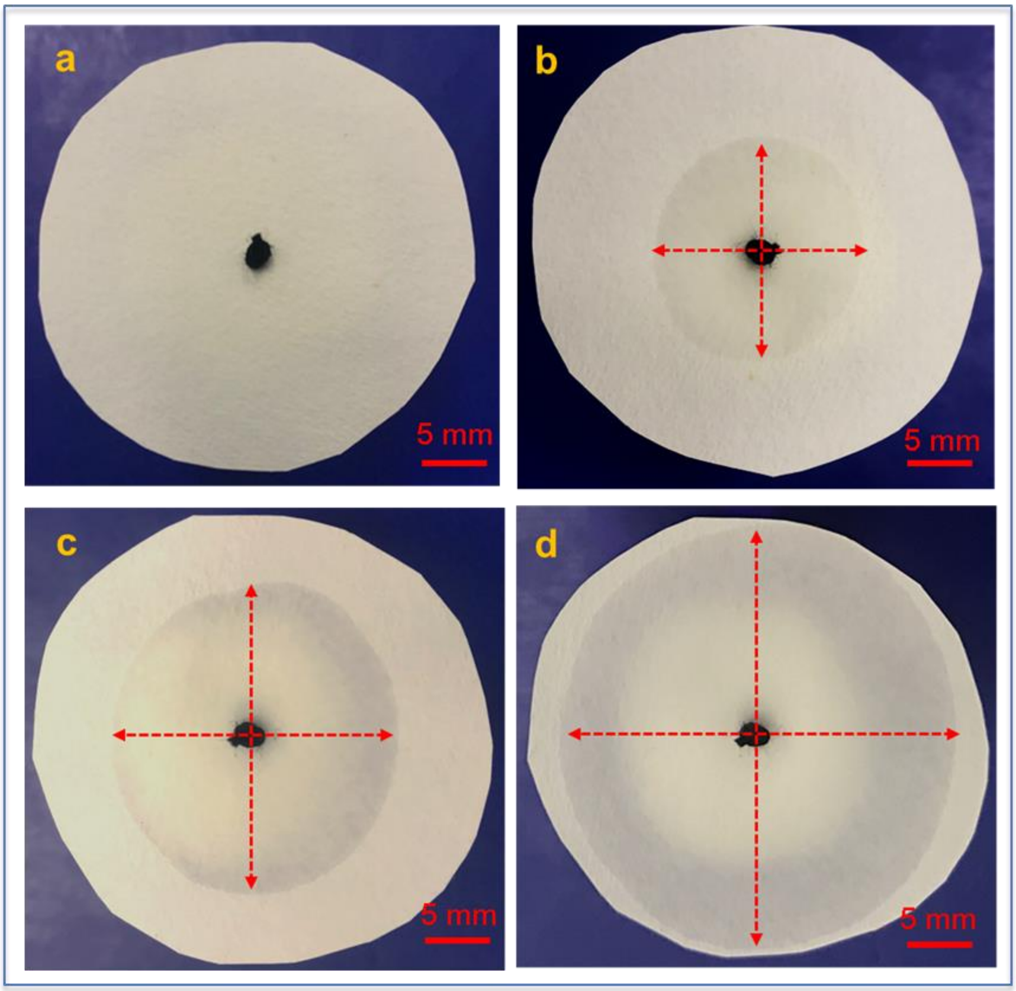

Fig. S6 The wetting process of the solution-spreading layer. a) b) c) and d) represent for the wetting state at 0, 1, 2 and 4 min, respectively. The red arrows are used to show the watermarks in the evaporation disc. The gradually expanding watermark from the centre suggests the radial solution transport direction.

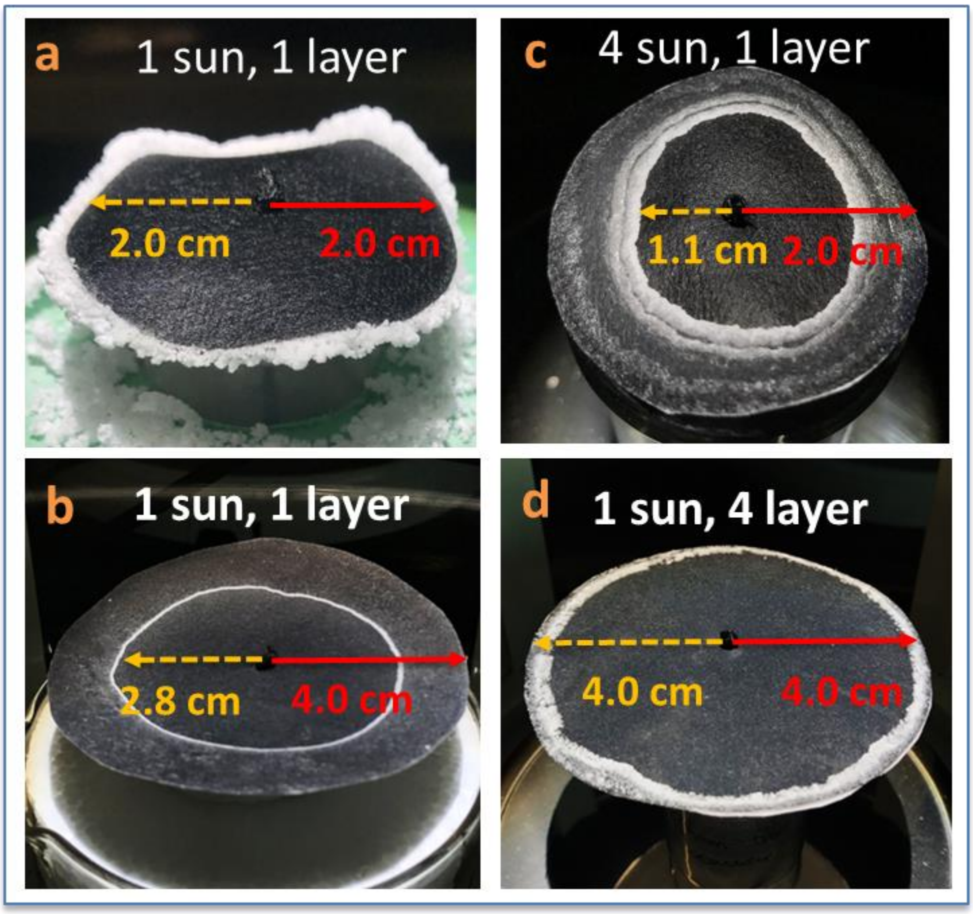

Fig. S7 Salt crystallization performance on of a) one layer of 4 cm disc under one sun, b) one layer of 4 cm disc under four sun, c) one layer of 8 cm disc under one sun and d) four layer of 8 cm disc under one sun. The red numbers and arrows represent for the radius of the disc, while the yellow ones are the mean radius of the salt ring. All the experiments employed 35 g/L NaCl solution as feed.

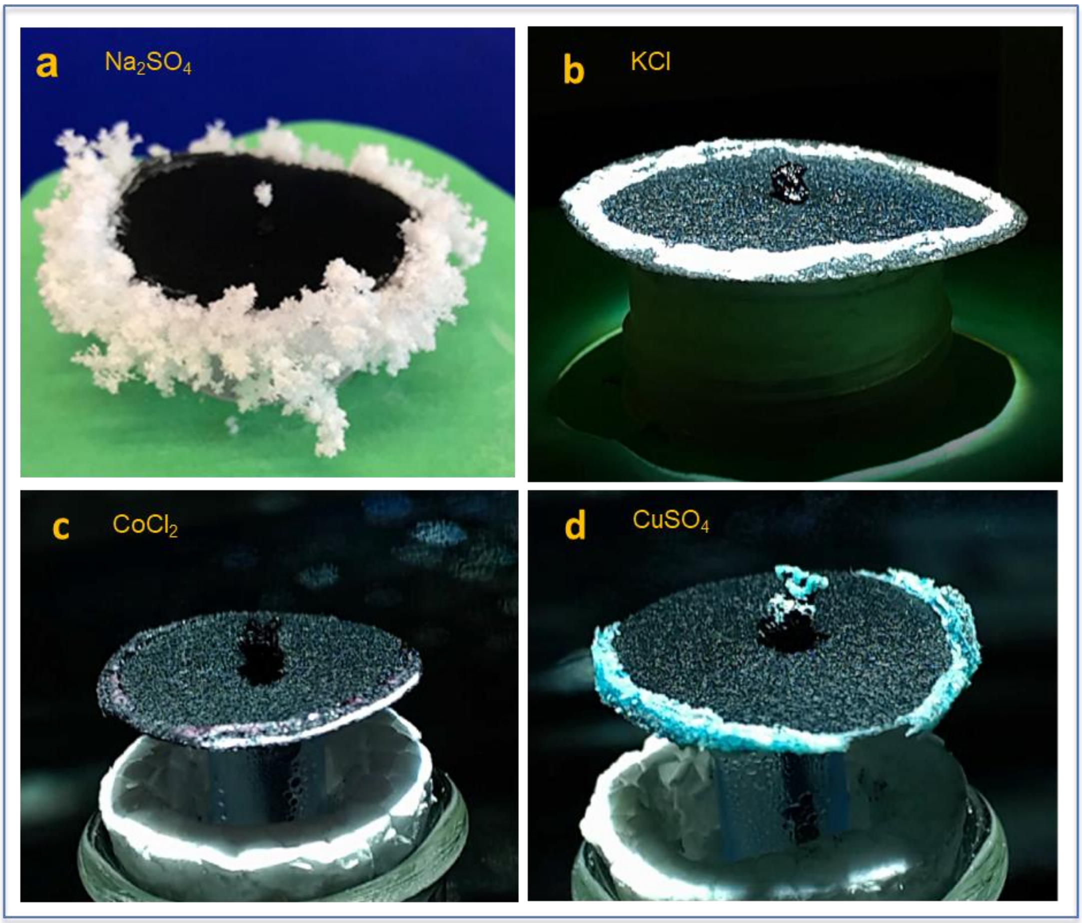

Fig. S8 Spatially separated salt crystallisation from water evaporation for other salts. a) 85.2 g/L Na_2SO_4 *solution with a 4 cm evaporation disc. b) 40 g/L KCl solution with a 4 cm evaporation disc. c) 1 g/L* $CoCl_2 \cdot 6H_2O$ *solution with 2 cm evaporation disc. d) 1 g/L* $CuSO_4 \cdot 5H_2O$ *solution with 2 cm evaporation disc. All these experiments were conducted under one sun irradiation.*

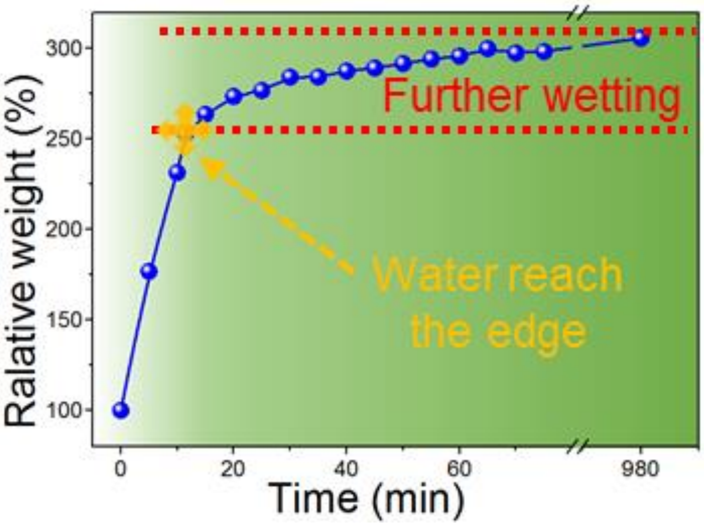

Fig. S9 Weight change profile in the wetting process of evaporation disc. The relative weight refers to the weight ratio of wet disc to dry disc. The linear increase of relative weight corresponds to the wetting process before water reaching the edge. The increased weight between the two dash lines is because of overnight wetting.

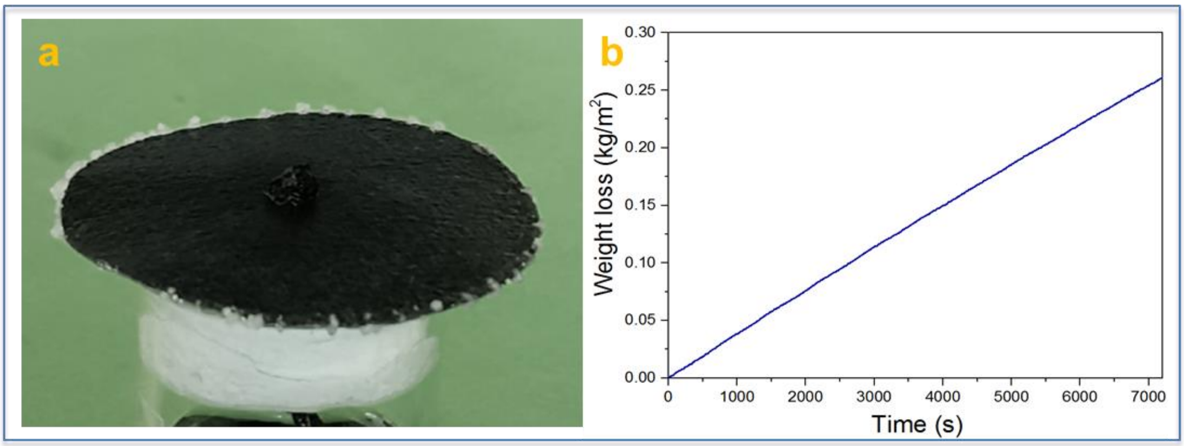

Fig. S10 Digital photograph of solar steam generation system prewetted with 35g/L NaCl in the dark condition. The white dots at the edge of the disc were seed crystals. b) Weight loss profile of the solar steam generator with 35 g/L NaCl solution in the dark condition. According to this curve, the evaporation rate in this condition is 0.13 kg/m^{2}h.

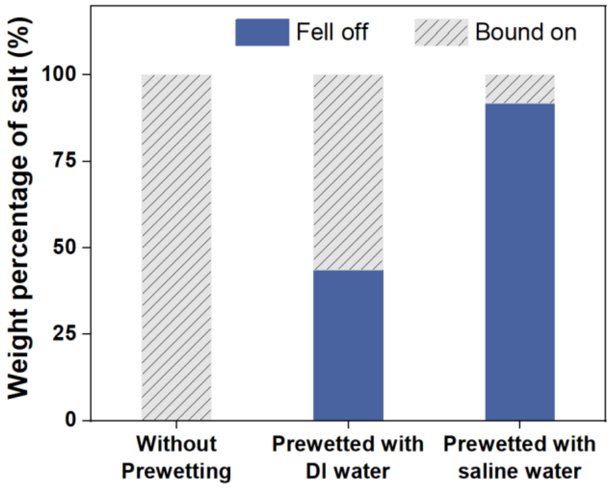

Fig. S11 The weight percentage of the salt crystals fell off and bound on the evaporation disc at varying wetting conditions after 24 h continuous operation.

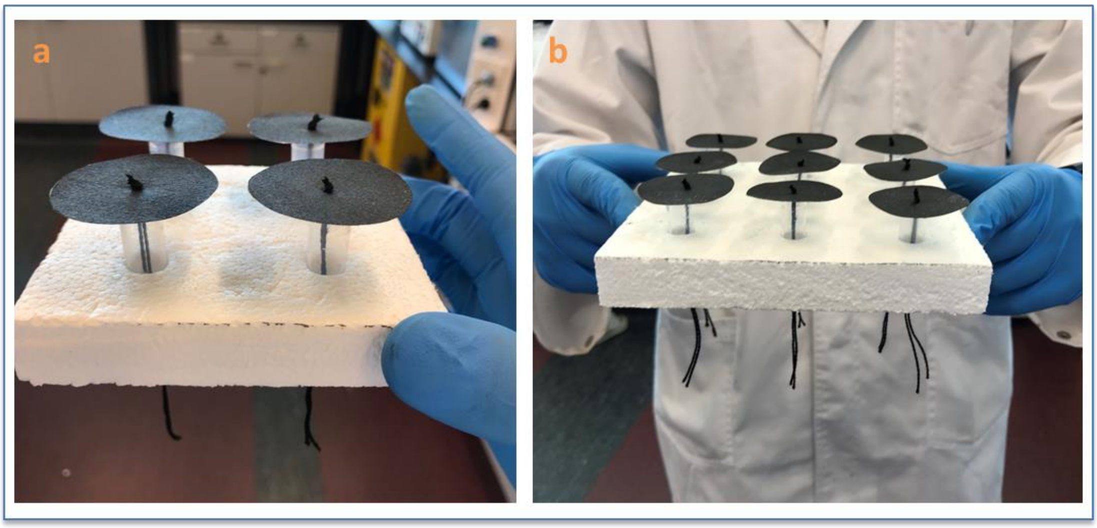

Fig. S12 The demonstration of scale-up methodology. a) 2×2 array of 4 cm discs. b) 3×3 array of 4 cm discs.

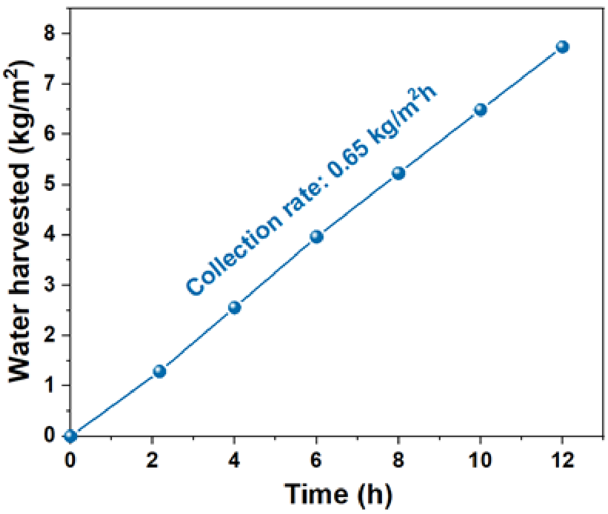

Fig. S13 The amount of collected water as a function of time. The device array composed of thirteen 1.8 cm devices was used as the solar steam generator, and a glass dome was placed above the device to condense the steam. The solar light intensity was calibrated to 1 kW/m^2 before covering the glass dome.

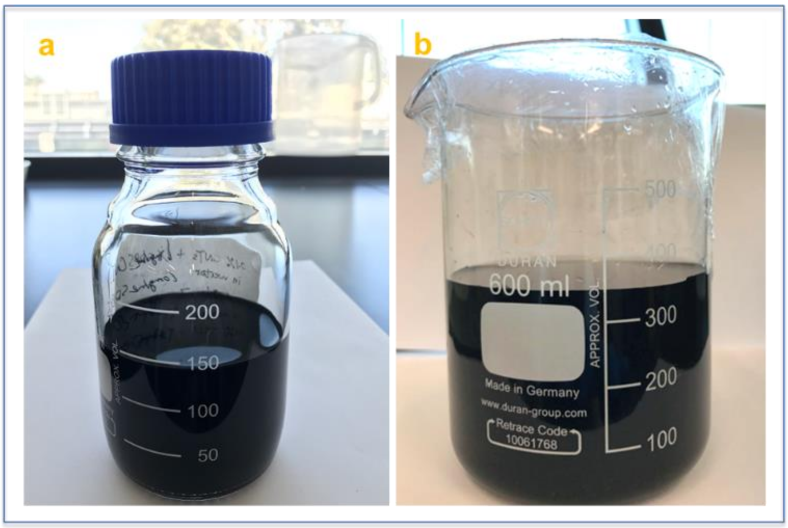

Fig. S14 Preparing CNTs suspension. a) Digital image of 1000 mg/L CNTs suspension in water. The super dark colour suggests excellent and broadband light absorption. The CNTs suspension remained stable after sitting for over one month. b) Digital image of ~10 mg/L CNTs suspension prepared from the 1000 mg/L CNTs suspension. The colour of the suspension was still dark even at low concentration, suggesting very good dispersion state of CNTs.

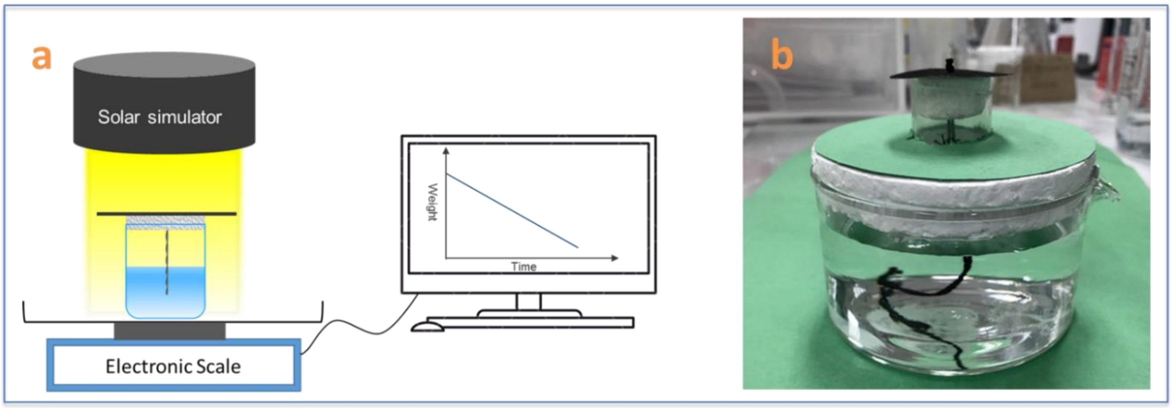

Fig. S15 a) Experimental setup used for measuring the evaporation rate. The reading was collected every 10 seconds by the A&D WinCT software. b) Experimental setup for salt harvesting experiment. A larger beaker was employed to supply sufficient amount of solution, and a polystyrene cover was used to prevent evaporation from the water surface.

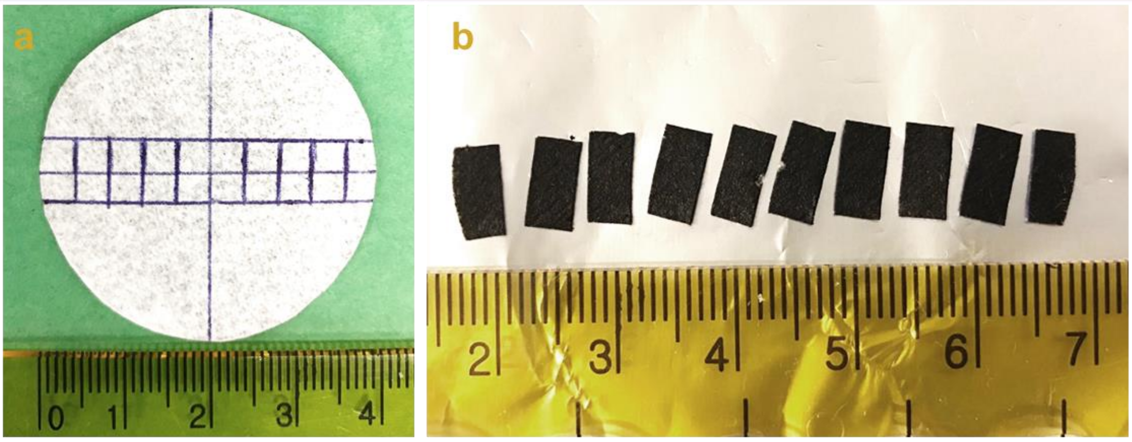

Fig. S16 Procedures for measuring salt concentration distribution. a) The grid on the back of evaporation disc. b) All the flakes for area measurement. They were cut according to the grid as shown in a).

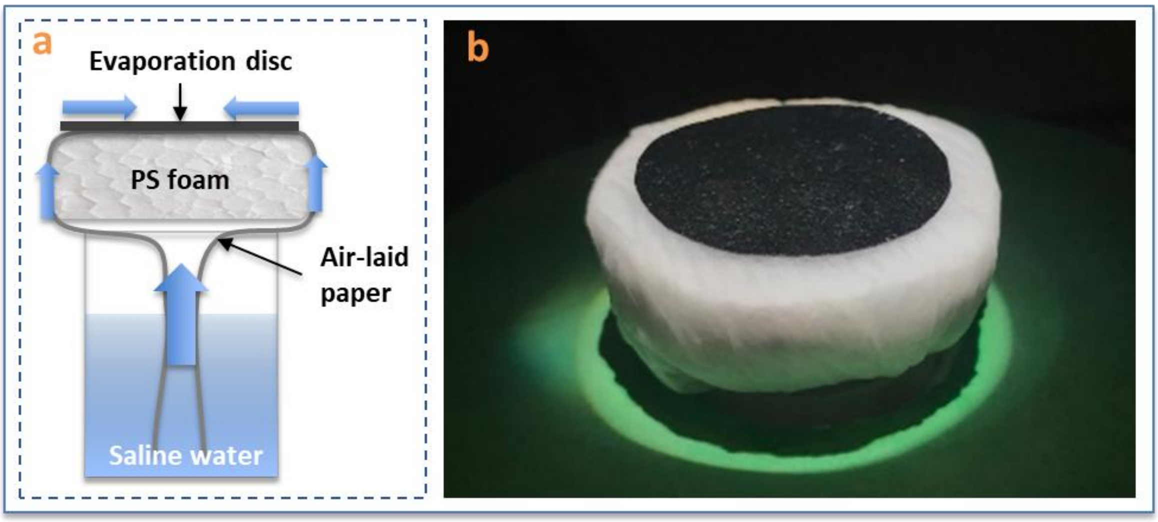

Fig. S17 Control experiment for Long-time water evaporation performance. a) The configuration of the control device. b) Digital photograph of the control experiment.

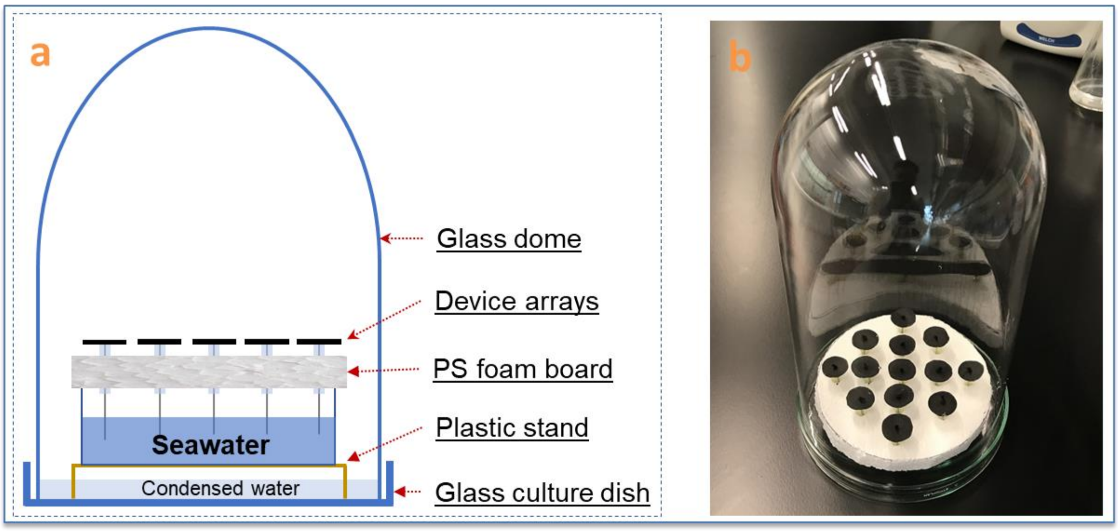

Fig. S18 Experimental setup for water collection. A) The design scratch and b) The digital photograph.

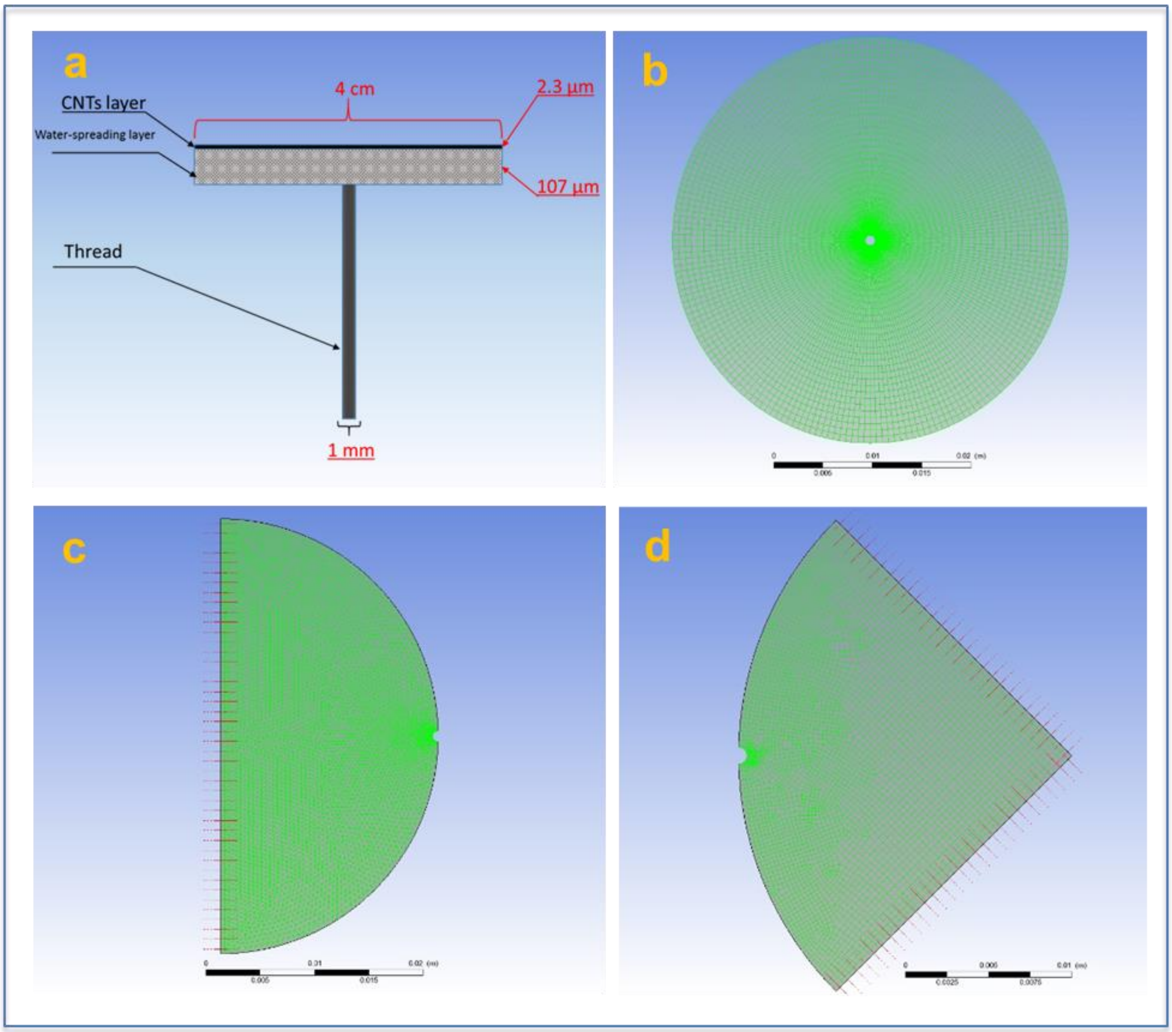

Fig. S19 The geometry of one-inlet configuration (a) and mesh used in CFD modelling for one-inlet (b), two-inlet (c) and four-inlet (d) configurations.

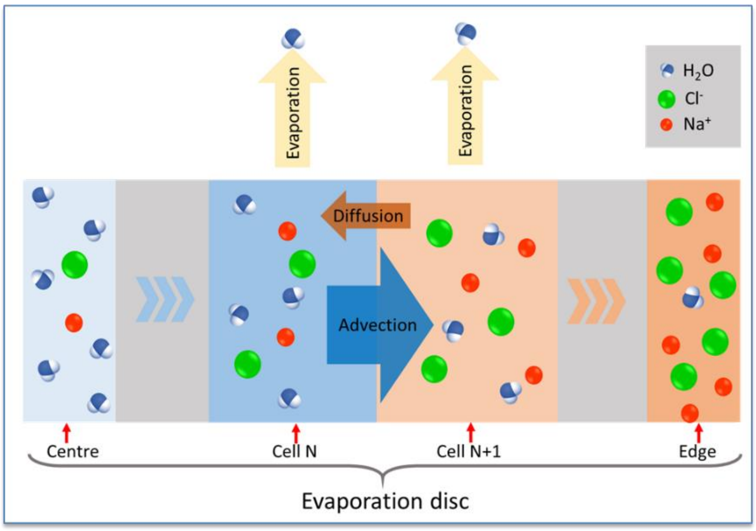

Fig. S20 Illustration of the process of water and salt transport from the centre to the edge. The evaporation disk was divided into an unlimited number of cells. The mass transfer of cell N includes three parts: advection, diffusion and evaporation

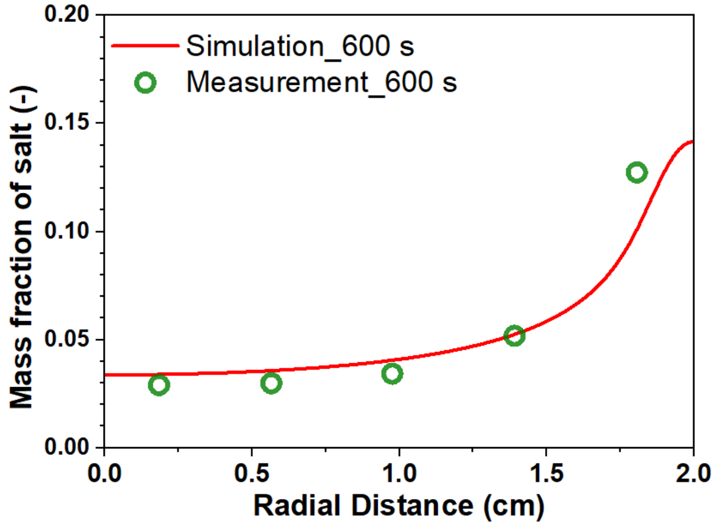

Fig. S21 Salt distribution on the evaporation disc after running for 600 s. The green dots are experimental measurements, and the red solid line is simulated results from the numerical calculation.

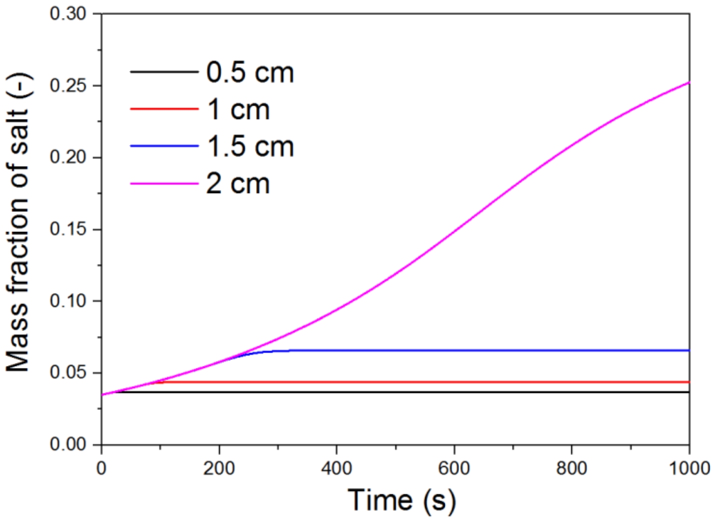

Fig. S22 The salt accumulating profile of the evaporation disc at different positions from the numerical simulation. The steep increase of salt concentration at the initial stage is mainly because of the fast advection, while the stable period after that is due to the salt diffusion. The concentration difference between these four positions becomes bigger and bigger.

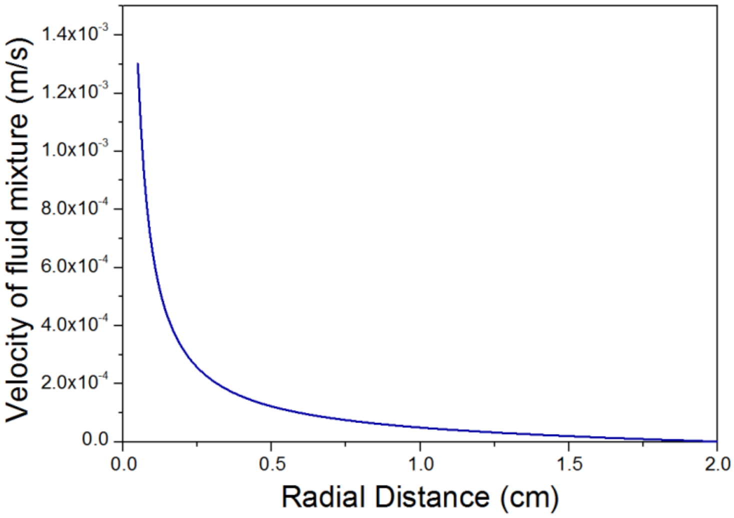

Fig. S23 Velocity profile of the fluid mixture presented against radial distance in numerical simulation for the one-thread configuration. The velocity of the fluid decreases exponentially with the radial distance.

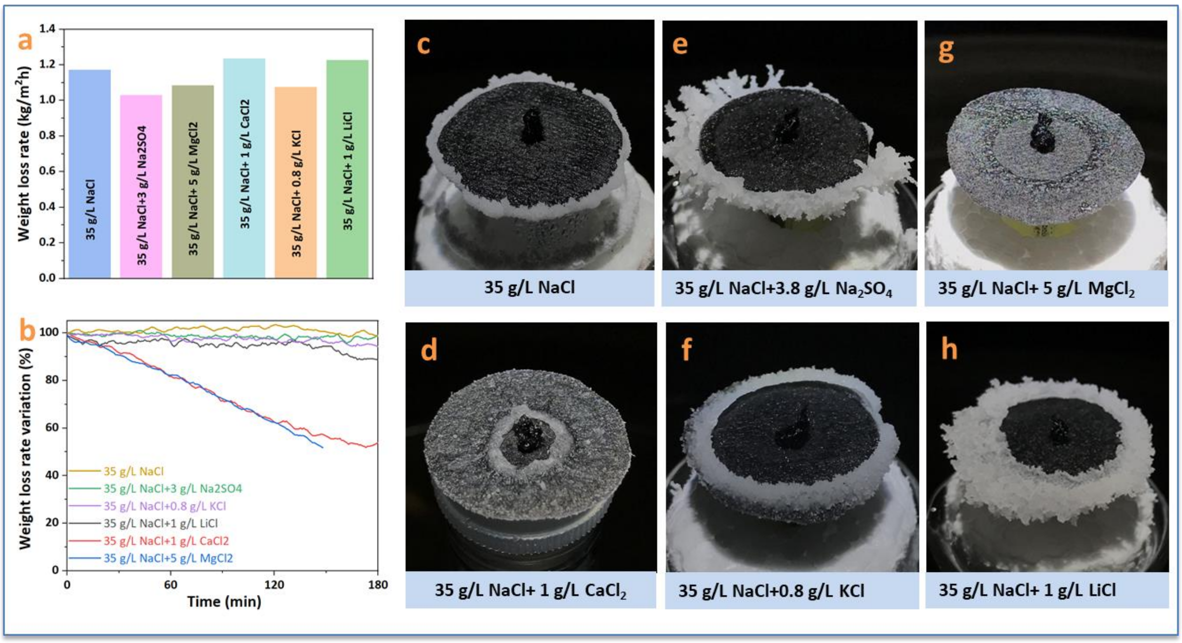

Fig. S24 The solar steam generation and salt crystallization performance in the presence of different salts. a) The starting rate of solar steam generation with mixed salt solutions. b) The variation of solar steam generation with mixed salt solutions. c)-h) The salt crystallization performance with mixed salt solutions.

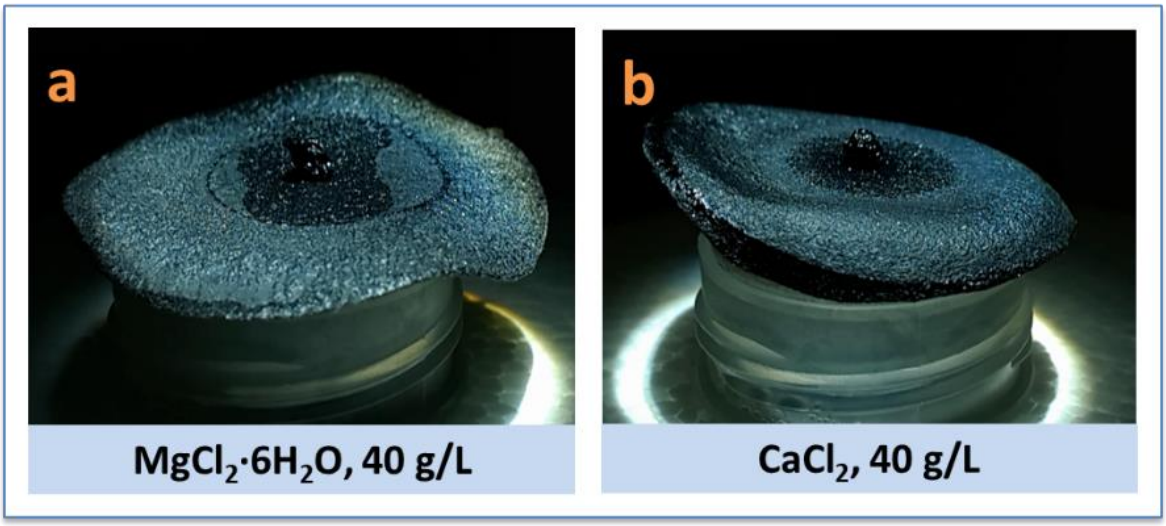

Fig. S25 The long-term evaporation performance of a) $MgCl_2$ and b) $CaCl_2$ solution.

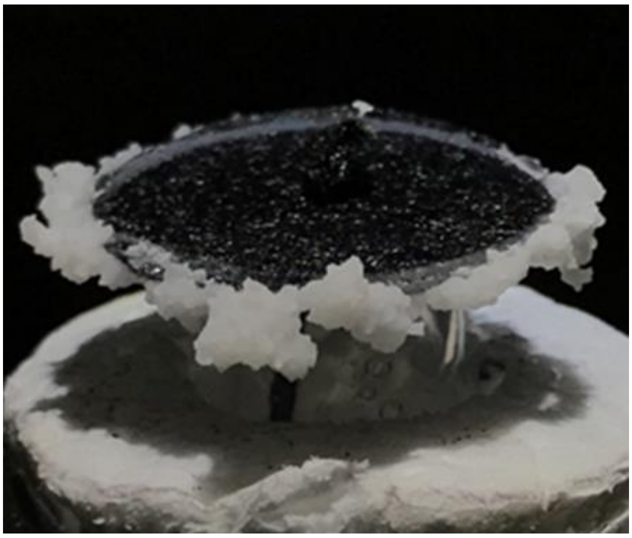

Fig. S26 The salt crystallization performance with pre-treat seawater.

7. Reference

1. Z. Sun, V. Nicolosi, D. Rickard, S. D. Bergin, D. Aherne and J. N. Coleman, J. Phys. Chem. C, 2008, **112**, 10692-10699.
2. X. Xie, M. Ye, L. Hu, N. Liu, J. R. McDonough, W. Chen, H. N. Alshareef, C. S. Criddle and Y. Cui, Energ. Environ. Sci., 2012, **5**, 5265-5270.
3. H. W. Chung, K. G. Nayar, J. Swaminathan, K. M. Chehayeb and J. H. Lienhard V, Desalination, 2017, **404**, 291–303.
4. V. Vitagliano and P. A. Lyons, J Am Chem Soc, 1956, **78**, 1549-1552.
5. J. Bear, Dynamics of fluids in porous media, Courier Corporation, 2013.
6. J. Floor Anthoni, (2000/2006) Oceanic Abundance of Elements. Available online at: www.seafriends.org.nz/oceano/seawater.htm (Accessed: 14 February 2019).
7. *Beijing Petroleum Engineering Corporation, Chlor-Alkali Industry Physics and Chemical Constant Data Manual, Beijing: Chemical Industry Press, 1988.*
8. *Y. Marcus, J. Chem. Soc. Faraday Trans., 1991,* ***87****(18), 2995-2999.*
9. *R.D. Shannon, Acta Crystallogr. A, 1976,* ***32****(5), 751-767.*